

Efficient Unrolled Networks for Large-Scale 3D Inverse Problems

Romain Vo Julián Tachella
 CNRS, ENS de Lyon, Laboratoire de Physique, Lyon, France
 roman.vo@ens-lyon.fr julian.tachella@ens-lyon.fr

Abstract

Deep learning-based methods have revolutionized the field of imaging inverse problems, yielding state-of-the-art performance across various imaging domains. The best performing networks incorporate the imaging operator within the network architecture, typically in the form of deep unrolling. However, in large-scale problems, such as 3D imaging, most existing methods fail to incorporate the operator in the architecture due to the prohibitive amount of memory required by global forward operators, which hinder typical patching strategies. In this work, we present a domain partitioning strategy and normal operator approximations that enable the training of end-to-end reconstruction models incorporating forward operators of arbitrarily large problems into their architecture. The proposed method achieves state-of-the-art performance on 3D X-ray cone-beam tomography and 3D multi-coil accelerated MRI, while requiring only a single GPU for both training and inference.

1. Introduction

Linear inverse problems are ubiquitous in science and engineering, with applications ranging from medical imaging to astronomy and remote sensing. These problems typically involve recovering an unknown signal $\mathbf{x}^* \in \mathbb{R}^n$ from noisy linear measurements $\mathbf{y} \in \mathbb{R}^m$ obtained via a known linear operator $\mathbf{A} \in \mathbb{R}^{m \times n}$:

$$\mathbf{y} = \mathbf{A}\mathbf{x}^* + \boldsymbol{\varepsilon}, \quad (1)$$

where $\boldsymbol{\varepsilon}$ represents measurement noise. Such problems are often ill-posed due to the lack of observed data, necessitating the use of regularization techniques to ensure stable and meaningful solutions.

In recent years, deep learning has emerged as a powerful tool for solving inverse problems, leveraging large datasets [31, 69] to learn complex mappings from measurements to signals. Notable approaches include *post-processing* methods and *unrolled networks*, both of which are trained end-to-end and attempt to recover the Minimum Mean Squared Error estimator (MMSE) [41]. The former learns a direct

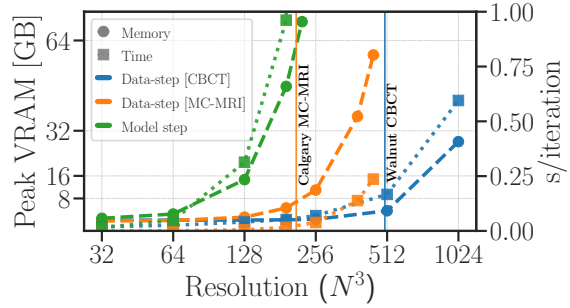


Figure 1. Peak video memory complexity (dashed lines) and global execution times (dotted lines) of isolated components used in unrolling. We show the cost of evaluating and back-propagating through a standard 3D data consistency step (using gradient descent) and a standard 3D network step (using a 3D DRUNet [72]). We see here that the bottleneck lies in the network step, which grows rapidly with the volume size, while the data-consistency step remains manageable even at high resolutions.

mapping between a low-quality reconstruction (typically the adjoint or linear pseudo-inverse reconstruction) and its ground-truth reference. While straightforward and effective, it often fails to enforce data-consistency, leading to reconstructions that may not align well with the observed measurements [23, 31, 38]. Unrolled networks, on the other hand, integrate knowledge of the forward operator \mathbf{A} into the reconstruction process by unrolling a fixed number of iterations of an optimization algorithm and replacing specific steps with learnable components [1, 2, 44, 53]. They demonstrate state-of-the-art performance across a wide range of benchmarks, combining the interpretability of traditional methods with the flexibility of deep learning.

However, incorporating global operators \mathbf{A} in the architecture requires training the network step at the full resolution. While in 2D problems this is typically feasible on a single GPU, the memory requirements of a global forward pass become prohibitive when working on 3D or higher dimensional problems, as illustrated in Fig. 1. Deep equilibrium training reduces the memory complexity of unrolled training to that of a single pass [4, 17, 19, 34]. Nonetheless, it still requires evaluating the full network at each iteration, which

is infeasible on a single GPU for large-scale 3D problems.

In this work, we address this scaling challenge by introducing two complementary techniques: domain partitioning and normal operator approximation. Domain partitioning enables us to decompose a large-scale inverse problem into smaller, more manageable subproblems, allowing us to adapt the network complexity to the available resources. This approach is inspired by patch-based training methods [46, 71], but extends them to the context of unrolled networks for the more challenging case where the forward operator is not trivially decomposable into patches (*e.g.* X-ray cone-beam CT). Normal operator approximation involves replacing $\mathbf{A}^\top \mathbf{A}$ by a product of diagonal and circulant matrices [49, 64], enabling efficient computation of data-consistency updates via the Fast Fourier Transform (FFT). By combining these techniques, we develop a framework that allows the training and deployment of unrolled networks for arbitrarily large linear inverse problems using only one GPU. This framework can be adapted to various types of linear operators. We demonstrate the effectiveness of our approach through extensive experiments on large-scale 3D inverse problems, showcasing state-of-the-art performance while significantly reducing memory and computational requirements. Our contributions are as follows:

- We propose a domain partitioning strategy of the operator \mathbf{A} that enables the training of unrolled networks on small patches, facilitating scaling to large problems.
- We introduce a normal operator approximation technique that leverages diagonal and circulant matrix products for efficient data-consistency updates. Notably, we show that the parameters of the factorization can be recovered efficiently by gradient descent without problem-specific data.
- We validate our approach on large-scale 3D inverse problems, namely Multi-Coil Magnetic Resonance Imaging (MC-MRI) and Cone-Beam X-ray Computed Tomography (CBCT). We demonstrate competitive performance with reduced resource consumption, *e.g.* handling up to 501^3 volumes on a single GPU.

2. Related work

Post-processing. Also called *artifact removal* or *restoration* network, a straightforward approach to building a reconstruction function is to learn a one-pass mapping between a low-quality reconstruction and its ground-truth reference [21, 30]. State-of-the-art post-processing techniques rely on widespread architectures to perform the reconstruction, *e.g.* UNet-based networks [46] and residual convolutional networks [72]. The most recent developments focus on transformer-based architectures [12, 68], which provide better performance in the high-data regime. While simple in design, post-processing scales well to large problems by leveraging patch-based training [71]. However, it does not

leverage the knowledge of the forward operator, which can lead to reconstructions that are not data-consistent and is not well-suited for problems where the acquisition conditions, represented by \mathbf{A} , may vary [32, 60].

Learned priors. Instead of handcrafting a regularization term, data-driven approaches [35, 38] use deep neural networks to learn the prior from data. In particular, Plug-and-Play (PnP) approaches [55, 63] leverage off-the-shelf denoisers to replace the *prior* step in iterative optimization algorithms. More recently, denoising diffusion models [24] have also been used as priors in inverse problems, leveraging their strong generative capabilities [7, 51, 74]. Due to their reliance on pre-trained networks, these methods can scale relatively well to large-scale problems, *i.e.* by trading off speed for memory [65]. Nonetheless, they are prone to instabilities [8, 43], and typically obtain worse MSE than unrolled networks trained in an end-to-end fashion. Moreover, in the case of 3D problems, pre-trained denoisers are often limited to 2D networks, which do not leverage the 3D structure of the data.

Unrolling. The core idea of unrolling is to transform a fixed number of optimization iterations into a network architecture, with the prior step parameterized as a learnable component [1, 3]. As opposed to PnP, an unrolled network is trained end-to-end for the specific inverse problem, which generally leads to better performance [31, 66]. However, unrolled methods are limited in practice to small-scale problems due to the high memory consumption required for storing all intermediate activations during training. This is especially true for 3D problems, where the memory consumption of the network step explodes and largely dominates that of the data-consistency step (Fig. 1). To alleviate this issue, some works have proposed to use reversible networks [47, 48], sketching [59], or checkpointing [22, 26]. Nonetheless, these approaches have yet to be sufficient to train unrolled networks on real-world 3D problems ($\approx 512^3$ voxels reconstructions) with global operators, *i.e.* operators acting on the entire volume.

Implicit neural representations (INR). Popularized by recent advances in computer graphics [37, 40] and also known as *neural fields*, INRs consist in representing a signal as a continuous function parameterized by a neural network [58, 67]. They generally require fewer parameters than traditional discrete representations, making them appealing for large-scale 3D problems [50, 56, 65, 70]. INRs are usually optimized per-sample using gradient-descent based algorithms, *i.e.* a separate network representation is trained for each test sample [67], which limits their applicability in large-scale inverse problems. They also tend to yield subpar results compared to standard feed-forward networks, as they do not leverage prior knowledge from data. Indeed, they fail to thoroughly address the scalability issues in large-scale

problems, as efficiently learning a prior over INRs requires training a network in weight space, which remains a significant challenge [13].

Fast linear operator approximations. Matrix factorization techniques approximate a linear operator by a product of structured matrices [73], *e.g.* sparse, low-rank, or circulant matrices. This topic has been widely studied to reduce the computational burden of large-scale linear operators across various fields, including inverse problems [6, 14]. An example of interest is the factorization of the Discrete Fourier Transform matrix by the Fast Fourier Transform (FFT) algorithm, which reduces the evaluation to a product of sparse matrices [29]. Closely related to the method we propose, Schmid *et al.* [49] show that any square linear operator can be factored into a finite product of diagonal and circulant matrices. We build upon these results to efficiently approximate the normal operator $\mathbf{A}^\top \mathbf{A}$ of large-scale inverse problems as the product of two factors, enabling fast data-consistency updates during unrolled training.

Remark 2.1 *This work is still relevant in the context of matrix-free operators, which is the case for the inverse problems implemented in our experiments, i.e. we compute $\mathbf{A}\mathbf{x}$ and $\mathbf{A}^\top \mathbf{y}$ for any \mathbf{x} and \mathbf{y} without explicitly forming the matrices.*

3. Background

Variational approach. When an inverse problem is ill-posed, *i.e.* when $m \ll n$ or \mathbf{A} is ill-conditioned, a common approach to recover \mathbf{x}^* is to solve a regularized optimization problem of the form

$$\hat{\mathbf{x}} \in \arg \min_{\mathbf{x} \in \mathbb{R}^n} d(\mathbf{A}\mathbf{x}, \mathbf{y}) + \lambda g(\mathbf{x}), \quad \lambda > 0, \quad (2)$$

where d is a data consistency term and g a suitable regularization term. The data-fidelity term is typically chosen as the ℓ_2 norm, *i.e.* $d(\mathbf{A}\mathbf{x}, \mathbf{y}) = \frac{1}{2} \|\mathbf{A}\mathbf{x} - \mathbf{y}\|_2^2$, which corresponds to the negative log-likelihood of the measurements under the Gaussian noise assumption. The regularization term encodes prior knowledge on the unknown signal, such as sparsity in a given basis [36] or smoothness [18].

Post-processing. Let us denote by \mathbf{D}_ϕ a deep neural network with parameters ϕ . Post-processing methods aim to learn a direct mapping from a fast, low-quality reconstruction, *e.g.* $\mathbf{A}^\top \mathbf{y}$ or $\mathbf{A}^\dagger \mathbf{y}$, to the ground-truth signal \mathbf{x}^* . When dealing with large volumes, *e.g.* 512^3 voxels, a popular approach is to leverage patch-based processing to mitigate the cost of training:

$$\mathcal{L}_{\text{POST}}(\phi) = \mathbb{E}_{\mathbf{S}} \mathbb{E}_{\mathbf{x}^*, \mathbf{y}} \|\mathbf{D}_\phi(\mathbf{S}\mathbf{x}_0) - \mathbf{S}\mathbf{x}^*\|_2^2, \quad (3)$$

where $\mathbf{x}_0 = \mathbf{A}^\top \mathbf{y}$ or $\mathbf{A}^\dagger \mathbf{y}$ can be pre-computed before training, and $\mathbf{S} \in \mathbb{R}^{p \times n}$ is the random linear operator that extracts patches in \mathbb{R}^p during training.

Unrolled methods.

Deep unrolled or deep unfolded optimization [1, 11, 53] can be seen as a form of data-driven regularization. The general idea is to replace the hand-crafted regularization term g by a learnable prior, parameterized by a deep neural network and trained end-to-end as part of an iterative procedure. It produces state-of-the-art results with fewer iterations than PnP methods [28].

Proximal Gradient Descent (PGD) [9] is a popular choice for unrolling, where the proximal step is replaced by a learned operator

$$\mathbf{x}_{k+1} = \mathbf{D}_\phi \left(\mathbf{x}_k - \eta \nabla_{\mathbf{x}_k} d(\mathbf{A}\mathbf{x}_k, \mathbf{y}) \right), \quad \eta > 0. \quad (4)$$

The reconstruction function $\mathbf{R}_\phi : \mathbb{R}^m \times \mathbb{R}^{m \times n} \rightarrow \mathbb{R}^n$ is defined as the output of K iterations of the procedure and is trained to minimize the following loss:

$$\begin{aligned} \mathcal{L}_{\text{UNR}}(\phi) &= \mathbb{E}_{\mathbf{x}^*, \mathbf{y}} \|\mathbf{R}_\phi(\mathbf{y}, \mathbf{A}) - \mathbf{x}^*\|_2^2 \\ \text{with } \mathbf{R}_\phi(\mathbf{y}, \mathbf{A}) &= \mathbf{x}_K(\phi), \quad \mathbf{x}_0 = \mathbf{A}^\top \mathbf{y} \text{ or } \mathbf{A}^\dagger \mathbf{y}. \end{aligned} \quad (5)$$

While post-processing networks (3) can be easily scaled to large 3D volume by training on smaller patches (e.g. 64^3 voxels), this simple idea does not apply to unrolled networks (4), which require training on full volumes.

More specifically, gradient computation during post-processing training does not involve the normal operator $\mathbf{A}^\top \mathbf{A}$:

$$\nabla_\phi \mathcal{L}_{\text{POST}} = \frac{\partial \mathcal{L}_{\text{POST}}}{\partial \hat{\mathbf{x}}}^\top \frac{\partial \mathbf{D}_\phi}{\partial \phi} \Big|_{\mathbf{x}_0}. \quad (6)$$

On the other hand, the gradient $\nabla_\phi \mathcal{L}_{\text{UNR}}$ accumulates contributions from all iterations, especially the data-step, which requires the full volume to be evaluated:

$$\begin{aligned} \frac{\partial \mathcal{L}_{\text{UNR}}}{\partial \mathbf{x}_{k+1}} &= \frac{\partial \mathcal{L}_{\text{UNR}}}{\partial \mathbf{x}_K} \prod_{j=k+1}^{K-1} \frac{\partial \mathbf{x}_{j+1}}{\partial \mathbf{x}_j}, \\ \text{with } \frac{\partial \mathbf{x}_{j+1}}{\partial \mathbf{x}_j} &= \frac{\partial \mathbf{D}_\phi}{\partial \mathbf{x}_j} (\mathbf{I} - \eta \mathbf{A}^\top \mathbf{A}). \end{aligned} \quad (7)$$

Block-separable inverse problems Consider a non-overlapping decomposition of the signal $\mathbf{x} = [\mathbf{x}_0^\top, \dots, \mathbf{x}_B^\top]^\top$, $\mathbf{x}_b \in \mathbb{R}^{n_b}$. If \mathbf{A} admits a block-diagonal structure then the following can be evaluated efficiently:

$$\begin{aligned} \mathbf{A}_b \mathbf{x}_b &= \mathbf{y}_b + \boldsymbol{\varepsilon}_b, \quad \mathbf{A}_b \in \mathbb{R}^{m \times n_b}, \quad \forall b \in \llbracket 1, B \rrbracket \\ \mathbf{A}\mathbf{x} &= [(\mathbf{A}_0 \mathbf{x}_0)^\top, \dots, (\mathbf{A}_B \mathbf{x}_B)^\top]^\top. \end{aligned} \quad (8)$$

When dealing with large-scale problems, such a decomposition allows breaking down the reconstruction task into B smaller problems that can be solved independently. For deep learning applications [54], a particularly interesting decomposition is one where each subspace \mathbb{R}^{n_b} , preferably with $n_b \ll n$, corresponds to a rectangular or cuboid patch of the original volume.

$$\hat{\mathbf{x}}_b = \mathbf{R}_\phi(\mathbf{y}_b, \mathbf{A}_b) \quad \forall b \in \llbracket 1, B \rrbracket, \quad \hat{\mathbf{x}} = \sum_{b=1}^B \mathbf{S}_b^\top \hat{\mathbf{x}}_b, \quad (9)$$

where $\mathbf{S}_b \in \mathbb{R}^{n_b \times n}$ is the selection operator that extracts the b -th patch from the full volume. However, such a decomposition does not often exist in real-world scenarios, especially in the case of 3D problems where the forward operator often couples all the voxels together. In Sec. 4, we propose two strategies to alleviate this issue, independently of the existence of a coordinate-friendly decomposition.

4. Method

In this section, we present a novel approach to scale unrolled networks to arbitrarily large linear inverse problems. We first introduce a **domain partitioning strategy** that allows us to reduce the size of the problem at train-time, which in turn permits the use of arbitrarily small networks that fit with memory constraints. Second, we introduce an **approximation** of the normal operator $\mathbf{A}^\top \mathbf{A}$ as a **product of diagonal and circulant matrices** that allows to compute sub-domains in a memory efficient manner. Relying on efficient implementations of the FFT, this approximation allows a significant speed-up of the data-consistency update. A circulant matrix evaluation can be performed exactly as a diagonal product in Fourier. We first present each technique independently, then discuss how they can be combined to solve large-scale 3D inverse problems.

4.1. Domain partitioning

Consider the decomposition of \mathbb{R}^n into 2 orthogonal subspaces

$$\mathbb{R}^n = \mathbb{R}^p \oplus \mathbb{R}^q \quad \text{with } q = n - p. \quad (10)$$

We define the matrices $\mathbf{S} \in \mathbb{R}^{p \times n}$ and $\mathbf{S}_\perp \in \mathbb{R}^{q \times n}$ which extracts a vector in \mathbb{R}^p , respectively in \mathbb{R}^q , from \mathbb{R}^n .

Using this decomposition, we assume that when solving the problem in (1), we already have part of the solution, *i.e.* instead of seeking $\mathbf{x}^* \in \mathbb{R}^n$, we want to recover the unknown $\mathbf{x}_{\text{patch}} \in \mathbb{R}^p$ such that

$$\mathbf{x}^* = \mathbf{S}^\top \mathbf{x}_{\text{patch}} + \mathbf{S}_\perp^\top \mathbf{x}_{\text{context}}, \quad (11)$$

where $\mathbf{x}_{\text{context}} \in \mathbb{R}^q$ is known. Typically, we choose $\mathbf{x}_{\text{patch}}$ as a rectangular or cuboid patch. This allows us to rewrite the linear system in (1) as

$$\tilde{\mathbf{y}} = \tilde{\mathbf{A}} \mathbf{x}_{\text{patch}}, \quad (12)$$

where $\tilde{\mathbf{A}} = \mathbf{A} \mathbf{S}^\top$ and $\tilde{\mathbf{y}} = \mathbf{y} - \mathbf{A} \mathbf{S}_\perp^\top \mathbf{x}_{\text{context}}$.

Figure 2. Domain partitioning strategy: in case of a forward operator \mathbf{A} that mixes the signal \mathbf{x} in a non-trivial manner, we can still decompose the full domain \mathbb{R}^n into two orthogonal subspaces \mathbb{R}^p and \mathbb{R}^q . Then by linearity, we solve for the unknown smaller patch $\mathbf{x}_{\text{patch}} \in \mathbb{R}^p$ (red) given the context $\mathbf{x}_{\text{context}} \in \mathbb{R}^q$ (blue).

We use the decomposition in (12) to reduce the large-scale problem into arbitrarily small ones. In the context of supervised learning, we choose $\mathbf{x}_{\text{context}} = \mathbf{S}_\perp \mathbf{x}^*$. Akin to patch-based training, we vary the position of the subspace \mathbb{R}^p at random and minimize the following loss:

$$\mathcal{L}_{\text{PART}}(\phi) = \mathbb{E}_{\mathbf{S}} \mathbb{E}_{\mathbf{x}^*, \mathbf{y}} \| \mathbf{R}_\phi(\tilde{\mathbf{y}}, \tilde{\mathbf{A}}) - \mathbf{S} \mathbf{x}^* \|_2^2, \quad (13)$$

with $\tilde{\mathbf{A}} = \mathbf{A} \mathbf{S}^\top$, $\tilde{\mathbf{y}} = \mathbf{y} - \mathbf{A} \mathbf{S}_\perp^\top \mathbf{x}^*$,

where $\mathbf{S} \mathbf{x}^* \in \mathbb{R}^p$ is the ground-truth patch corresponding to the subspace \mathbb{R}^p .

Test-time without ground-truth context. We deploy the network \mathbf{R}_ϕ , trained with *domain partitioning*, in a two-step procedure:

1. At test-time, we can mitigate the complexity of evaluating the prior step \mathbf{D}_ϕ on the full volume by evaluating it sequentially along patches and merging the processed patches. Thus, we obtain an estimation $\tilde{\mathbf{x}}$ of the ground-truth signal by solving the full problem in (1). We use a standard unrolled scheme, denoted by $\tilde{\mathbf{x}} = \mathbf{R}_\phi(\mathbf{y}, \mathbf{A})$, where the data-step is computed on the whole volume, *i.e.* without partitioning, and the prior step \mathbf{D}_ϕ is performed patch-by-patch.
2. We use the estimation $\tilde{\mathbf{x}}$ to build a context within our *domain-partitioned* framework, *i.e.* $\mathbf{x}_{\text{context}} = \mathbf{S}_\perp \tilde{\mathbf{x}}$, and independently solve each subproblem using the same network \mathbf{R}_ϕ .

For the CBCT experiments, we observe that this two-step refining procedure consistently improves the reconstruction quality compared to using only the initial estimation $\tilde{\mathbf{x}}$. For the MC-MRI experiments, we observe that the first estimation $\tilde{\mathbf{x}}$ is already of high-quality, thus the second refinement step brings negligible improvements. A summary of the test-time algorithm is provided in Algorithm 1, and we give more details in Appendix B.

Algorithm 1: Test-time domain partitioned inference

init: $\mathbf{y} \in \mathbb{R}^m$, $\mathbf{A} \in \mathbb{R}^{m \times n}$, $\mathbf{x}_0 = \mathbf{A}^\dagger \mathbf{y} \in \mathbb{R}^n$,
 $k = 0$, $K > 0$, step size $\eta > 0$, \mathbf{R}_ϕ .

First unrolling procedure to get $\tilde{\mathbf{x}} \approx \mathbf{x}^*$

$\tilde{\mathbf{x}} \leftarrow \mathbf{R}_\phi(\mathbf{y}, \mathbf{A})$

Domain partitioned computation

$X_{\text{patches}} = []$

for S in patches () **do**

init: $\mathbf{x}_{\text{context}} = \mathbf{S}_\perp \tilde{\mathbf{x}}$, $\tilde{\mathbf{A}} = \mathbf{A} \mathbf{S}^\top$,
 $\tilde{\mathbf{y}} = \mathbf{y} - \mathbf{A} \mathbf{S}_\perp^\top \mathbf{S}_\perp \tilde{\mathbf{x}}$ (12)
 $\hat{\mathbf{x}}_{\text{patch}} \leftarrow \mathbf{R}_\phi(\tilde{\mathbf{y}}, \tilde{\mathbf{A}})$

 append (X_{patches} , $\hat{\mathbf{x}}_{\text{patch}}$)

$\hat{\mathbf{x}} \leftarrow \text{aggregate}(X_{\text{patches}})$

4.2. Normal operator approximation

We previously introduced the domain partitioning decomposition where $\tilde{\mathbf{y}} = \tilde{\mathbf{A}} \mathbf{x}_{\text{patch}}$ with $\tilde{\mathbf{A}} = \mathbf{A} \mathbf{S}^\top$. Note here that solving (12) still requires the global forward operator and its adjoint, *i.e.* through the evaluation of $\tilde{\mathbf{A}}^\top \tilde{\mathbf{A}} = \mathbf{S} \mathbf{A}^\top \mathbf{A} \mathbf{S}^\top$. In this section, we introduce an efficient approximation of the normal operator $\mathbf{A}^\top \mathbf{A}$ that significantly reduces the computational burden of naively evaluating $\tilde{\mathbf{A}}^\top \tilde{\mathbf{A}}$.

Let us recall the data-consistency update typically computed in the form of a gradient descent step:

$$\begin{aligned} h(\mathbf{x}) &= \mathbf{x} - \eta \nabla_{\mathbf{x}} d(\mathbf{A}\mathbf{x}, \mathbf{y}) \\ &= \mathbf{x} - \eta(\mathbf{A}^\top \mathbf{A})\mathbf{x} + \mathbf{A}^\top \mathbf{y}. \end{aligned} \quad (14)$$

Discarding the constant term $\mathbf{A}^\top \mathbf{y}$ which can be pre-computed, we see that a computing (14) only requires the evaluation of the normal operator $\mathbf{A}^\top \mathbf{A} \mathbf{x}$.

Remark 4.1 Focusing on the evaluation of the normal operator $\mathbf{A}^\top \mathbf{A}$ is not restrictive. In the case of the data consistency step being a proximal step, *i.e.* $h(\mathbf{x}) = \text{prox}_{\eta d(\mathbf{A}\cdot, \mathbf{y})}(\mathbf{x})$, $\mathbf{A}^\top \mathbf{A}$ is again the main component in most popular solvers, *e.g.* conjugate gradient.

Translation-equivariant operators. Assuming that \mathbf{A} is translation-equivariant, then $\mathbf{A}^\top \mathbf{A}$ is a convolutional operator [64]. In this case, we can leverage the convolution theorem to efficiently compute the normal operator evaluation in the Fourier domain. More precisely, we can write

$$\mathbf{A}^\top \mathbf{A} \mathbf{x} = \mathbf{F}^{-1} \text{diag}(\boldsymbol{\lambda}) \mathbf{F} \mathbf{x}, \quad (15)$$

where \mathbf{F} and \mathbf{F}^{-1} are the Fourier and inverse Fourier transforms, respectively, and $\boldsymbol{\lambda} \in \mathbb{C}^n$ is the frequency response of the convolution kernel associated with $\mathbf{A}^\top \mathbf{A}$.

Spatial modulation. We can generalize the factorization to a larger class of non-translation equivariant operators, *e.g.*

inpainting, by modulating the output of the convolution by a diagonal operation in the spatial domain. More precisely, we factorize the normal operator as

$$\mathbf{A}^\top \mathbf{A} = \mathbf{H} = \text{diag}(\mathbf{m}) \mathbf{F}^{-1} \text{diag}(\boldsymbol{\lambda}) \mathbf{F}, \quad (16)$$

where $\mathbf{m} \in \mathbb{R}^n$ is homogeneous to a spatial sensitivity map, or mask.

Following Schmid *et al.* [49], we could increase the expressivity of the approximation by adding more diagonal-circulant factors, *i.e.* $\mathbf{H} = \prod_{i=1}^N \text{diag}(\mathbf{m}_i) \mathbf{F}^{-1} \text{diag}(\boldsymbol{\lambda}_i) \mathbf{F}$. However, in practice we observe that a single factorization ($N = 1$) is sufficient to obtain good reconstruction results while keeping the computational cost low.

Remark 4.2 Note that in (16) we approximate the symmetric operator $\mathbf{A}^\top \mathbf{A}$ with a non-symmetric factorization \mathbf{H} . In practice, we observe that imposing symmetry constraints during the fitting procedure does not improve the quality of the approximation nor the final reconstruction results. At test-time, using either \mathbf{H} or its symmetrized version $\frac{1}{2}(\mathbf{H} + \mathbf{H}^\top)$ yields similar results, thus we keep the simpler version \mathbf{H} for efficiency.

Examples. For CT, the Fourier slice theorem states that each row of the forward operator corresponds to sampling a *radial* line in the Fourier domain [16], which is exactly written as a diagonal operation in frequency space. The spatial modulation $\text{diag}(\mathbf{m})$ can then be interpreted as a resampling map which compensates the *cartesian* sampling done by the FFT, rather than a *radial* computation. For other modalities, such as deconvolution problems, \mathbf{A} is exactly a convolutional operator and \mathbf{m} is simply an all-one vector. For inpainting problems, \mathbf{A} is a diagonal binary masking operator and $\mathbf{A}^\top \mathbf{A} = \mathbf{A}$, which can be exactly represented by our proposed form in (16) with $\boldsymbol{\lambda}$ being an all-one vector.

Remark 4.3 For multi-coil MRI, the normal operator writes $\mathbf{A}^\top \mathbf{A} = \sum_{c=1}^C \mathbf{S}_c^\top \mathbf{F}^{-1} \mathbf{M}^\top \mathbf{M} \mathbf{F} \mathbf{S}_c$, where \mathbf{S}_c is the sensitivity map of coil c and \mathbf{M} is the undersampling mask in frequency space. In this case, the normal operator cannot be exactly represented by our proposed form in (16). Indeed, the approximation breaks down to finding a single-coil equivalent of a multi-coil forward model. In practice, we observe that by slightly changing the factorization to $\mathbf{H} = \text{diag}(\mathbf{m})^H \mathbf{F}^{-1} \text{diag}(\boldsymbol{\lambda}) \mathbf{F} \text{diag}(\mathbf{m})$, we can obtain a good approximation of the multi-coil normal operator.

Fitting the approximation. We fit the parameters \mathbf{m} and $\boldsymbol{\lambda}$ by gradient descent on a set of random vectors $\{\mathbf{x}_i\}_{i=1}^N$. More precisely, we minimize the following loss:

$$\mathcal{L}(\mathbf{m}, \boldsymbol{\lambda}) = \mathbb{E}_{\mathbf{x} \sim \mathcal{N}(\mathbf{0}, \mathbf{I})} \|\mathbf{A}^\top \mathbf{A} \mathbf{x} - \mathbf{H}(\mathbf{m}, \boldsymbol{\lambda}) \mathbf{x}\|_2^2. \quad (17)$$

Using properties of standard Gaussian random vectors, note that (17) is equal to the Frobenius norm of the residual, *i.e.*

$$\begin{aligned}\mathcal{L}(\mathbf{m}, \boldsymbol{\lambda}) &= \mathbb{E}_{\mathbf{x} \sim \mathcal{N}(\mathbf{0}, \mathbf{I})} \|\mathbf{A}^\top \mathbf{A} \mathbf{x} - \mathbf{H}(\mathbf{m}, \boldsymbol{\lambda}) \mathbf{x}\|_2^2 \\ &= \|\mathbf{A}^\top \mathbf{A} - \mathbf{H}(\mathbf{m}, \boldsymbol{\lambda})\|_F^2\end{aligned}\quad (18)$$

This means that we can fit the parameters $(\mathbf{m}, \boldsymbol{\lambda})$ of the factorization without any problem-specific data, which is particularly useful when the forward operator \mathbf{A} is known but a limited amount of training data is available.

4.3. Efficient approximation on partitioned domain

When using the domain partitioning strategy presented in Sec. 4.1, we need to efficiently compute the normal operator evaluation on any patch $\mathbf{x}_{\text{patch}} \in \mathbb{R}^p$, *i.e.* $\tilde{\mathbf{A}}^\top \tilde{\mathbf{A}} \mathbf{x}_{\text{patch}} = \mathbf{S} \mathbf{A}^\top \mathbf{A} \mathbf{S}^\top \mathbf{x}_{\text{patch}}$. Using the approximation in (16), we can write

$$\tilde{\mathbf{A}}^\top \tilde{\mathbf{A}} \mathbf{x}_{\text{patch}} \approx \mathbf{S} \text{diag}(\mathbf{m}) \mathbf{F}^{-1} \text{diag}(\boldsymbol{\lambda}) \mathbf{F} \mathbf{S}^\top \mathbf{x}_{\text{patch}}. \quad (19)$$

Let us decompose (19) into finer steps: (i) $\mathbf{S}^\top \mathbf{x}_{\text{patch}}$ is a zero-padding operation, that materializes in memory a vector of size n , from a patch of size $p \ll n$, (ii) $\mathbf{F}^{-1} \text{diag}(\boldsymbol{\lambda}) \mathbf{F}$ is equivalent to a convolution with a kernel of size n , (iii) $\mathbf{S} \text{diag}(\mathbf{m})$ is a diagonal operator of size p .

Here, note that both steps (i) and (ii) are highly inefficient as they require going back to the full signal volume. As the input of the convolution is a zero-padded cuboid, we can restrict the convolution kernel to a smaller size $k = 2p \ll n$ and maintain exact computation. More precisely, we can write

$$\begin{aligned}\mathbf{S} \text{diag}(\mathbf{m}) \mathbf{F}^{-1} \text{diag}(\boldsymbol{\lambda}) \mathbf{F} \mathbf{S}^\top \mathbf{x}_{\text{patch}} \\ = \text{diag}(\mathbf{S} \mathbf{m}) \mathbf{F}_k^{-1} \text{diag}(\boldsymbol{\lambda}_k) \mathbf{F}_k \mathbf{x}_{\text{patch}},\end{aligned}\quad (20)$$

where \mathbf{F}_k and \mathbf{F}_k^{-1} are the Fourier and inverse Fourier transforms restricted to size k (with zero-padding or cropping from \mathbb{R}^p to \mathbb{R}^k), respectively, and $\boldsymbol{\lambda}_k \in \mathbb{C}^k$ is the frequency response of the convolution kernel restricted to size k .

5. Experiments

We conduct experiments on two large-scale 3D inverse problem modalities: X-ray Cone-Beam Computed Tomography (CBCT) and Multi-Coil Magnetic Resonance Imaging (MC-MRI). First, we evaluate the performance of our **domain partitioning** approach, which allows us to train unrolled networks on small patches while deploying them on the whole problem at test-time. Second, we assess the benefits of our **normal operator approximation** technique, which enables efficient data-consistency updates during unrolled training. **Baselines** As non-learned methods, we consider the Feldkamp-Davis-Kress (FDK) algorithm [15] for CBCT and the zero-filled root-sum-of-squares (RSS) reconstruction for MC-MRI. We also compare against Total Variation (TV)

minimization [18] as a standard variational method. For each dataset, we also compare against several deep learning-based baselines, representative of the prominent families of methods for inverse problems and also scalable to 3D (see Sec. 2): (i) post-processing networks [21, 30], which learn a one-pass mapping from a low-quality reconstruction to the ground-truth; (ii) PnP- α PGD [25, 63, 65] and DPIR [60, 72], (iii) unrolled networks [2, 3, 11, 53], and (iv) implicit neural representations with instantNGP [40]. We use tied-weights unrolled networks, with $K = 5$ iterations on the MC-MRI dataset, and $K = 3$ iterations on the CBCT dataset. Notably in the CBCT experiments, Tab. 1, the unrolled network with our strategy is trained with a batch of size 1, while all other learned methods use a batch size of 4, we accumulate gradients over 4 steps to match the effective batch size.

For all learned experiments, we fix the backbone architecture to a DRUNet [72], a residual UNet-like convolutional network with 36.2M parameters, widely used in inverse problems. When applicable, we report results for both 2D and 3D versions of the methods to highlight the benefits of leveraging the 3D structure of the data, rather than processing it slice-by-slice. The 3D counterpart of the DRUNet has approximately 96.5M parameters. The different methods are implemented in pytorch [42] and trained on a single H100 GPU with 80GB. We use the astra-toolbox [61, 62] and deepinverse [57] libraries for CBCT and MC-MRI operators. Additional implementation details are provided in Appendix A.

5.1. Cone-Beam Computed Tomography

Table 1. Reconstruction performances on the **Walnut-CBCT** dataset. We do not report results for the standard unrolled approach as training it is infeasible on a single GPU and yields *out of memory* errors (OOM). When applicable we report the peak GPU memory (VRAM) usage in gigabytes (GB) as well as the training speed in seconds per step (s/step). **Best** and **second-best** results highlighted.

Walnut-CBCT	SSIM \uparrow			PSNR \uparrow			VRAM \downarrow	train - s/step \downarrow
Views (/1200)	30	50	100	30	50	100		30, 50, 100
FDK	0.197	0.263	0.375	18.53	21.16	24.74	N/A	N/A
TV	0.799	0.850	0.893	27.88	29.72	31.63	N/A	N/A
INR [3D]	0.805	0.862	0.913	29.97	32.18	33.74	N/A	N/A
PnP- α PGD [2D]	0.805	0.875	0.889	28.74	32.15	33.97	11.94	0.07
PnP- α PGD [3D]	0.803	0.868	0.884	28.63	31.69	33.72	67.50	1.39
DPIR [RAMI][2D]	0.774	0.815	0.826	28.33	30.19	31.17	N/A	N/A
DRUNet[2D]	0.820	0.866	0.865	28.30	31.14	33.66	11.94	0.07
DRUNet[3D]	0.857	0.905	0.931	29.47	32.49	35.22	67.50	1.39
Unrolled[3D]	x	x	x	x	x	x	OOM	x
Unrolled[2D] - ours	0.855	0.911	0.942	29.37	32.52	35.79	15.17	2.56
Unrolled[3D] - ours	0.877	0.926	0.947	31.17	34.21	37.07	44.70	1.20 $\times 4$

CBCT is a typical example of a 3D inverse problem that does not admit a coordinate-friendly partitioning of the forward operator, thus making it impossible to train unrolled networks on patches without our proposed domain partitioning strategy.

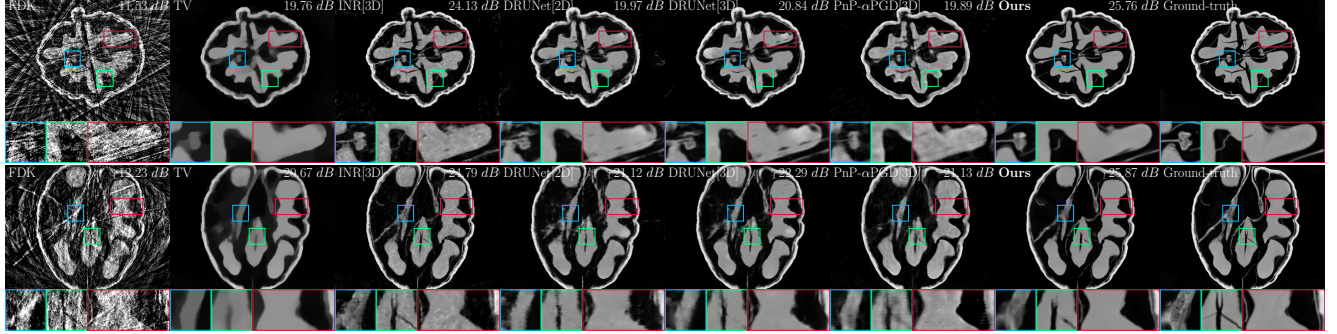


Figure 3. Illustrations of sparse view reconstructions with [30/1200] projections on the Walnut-CBCT [10] dataset using the methods compared in Tab. 1. *First row* axial slices, *second row* vertical slices from the same sample. PSNR is computed per slice.

We use real-world measurements from the **Walnut-CBCT** dataset [10], which contains high-resolution CBCT scans of several walnuts. The detector has a size of 972×768 and the reconstructed volumes have a size of 501^3 voxels. We simulate sparse-view CBCT by sub-sampling the projections to 30, 50, and 100 views out of the original 1200. During training, we use patches of size 384^2 when using a 2D DRUNet and 8×384^2 with a 3D DRUNet. For each experiment, we train simultaneously on the three sub-sampling configurations.

In Tab. 1, we see that our domain partitioning strategy combined with our normal operator approximation technique allows us to train an unrolled 3D DRUNet, which achieves the best reconstruction performance among all compared methods. In Tab. 3 we also demonstrate the individual benefits of our normal operator approximation technique, which significantly reduces the training time while boosting the performance.

5.2. Multi-Coil Magnetic Resonance Imaging

Table 2. Reconstruction performances on the **Calgary-Campinas** dataset. PSNR and SSIM are measured on amplitude images. *Best* and *second-best* results highlighted.

Calgary-Campinas	SSIM \uparrow		PSNR \uparrow		VRAM \downarrow	train - s/step \downarrow
	R=5	R=10	R=5	R=10		
Acceleration rate	R=5 & 10					
RSS	0.473	0.334	24.40	21.92	N/A	N/A
TV	0.790	0.726	32.42	30.23	N/A	N/A
INR [3D]	0.748	0.666	30.23	28.06	N/A	N/A
PnP- α PGD [2D]	0.639	0.661	27.08	28.70	10.04	0.080
PnP- α PGD [3D]	0.649	0.648	27.27	28.47	18.54	0.610
DPIR (RAM)[2D]	0.612	0.582	28.24	27.35	N/A	N/A
DRUNet[2D]	0.913	0.873	33.87	31.31	10.04	0.080
DRUNet[3D]	0.930	0.900	35.02	32.67	17.85	0.610
Unrolled[2D]	0.941	0.905	36.43	33.20	15.04	0.190
Unrolled[3D]	0.952	0.926	37.74	34.72	75.93	2.16
Unrolled[2D] - ours	0.942	0.906	36.61	33.26	11.66	0.590
Unrolled[3D] - ours	0.948	0.919	37.36	34.25	37.02	1.10

For the MC-MRI modality, we use real-world measurements from the **Calgary-Campinas** dataset [52], which contains

high-resolution multi-coil MRI scans of brains. The fully-sampled k-space data has a size of $256 \times 218 \times 170$ per coil, with 12 coils in total. We simulate accelerated MC-MRI by retrospectively undersampling the k-space with acceleration rates of 5 and 10 using a Poisson-disc sampling pattern [52]. For each experiment, we train simultaneously on both acceleration configurations.

As opposed to the CBCT experiments, the underlying Fourier operator in the **Calgary-Campinas** dataset uses a Cartesian sampling pattern, which admits a coordinate-friendly partitioning along the depth dimension. This makes it possible to solve the 3D problem by solving a set of independent, smaller problems. Therefore, we also train an unrolled network on plain 2D slices or small 3D volumes truncated in the depth dimension. Using our domain partitioning strategy, we show that we can further reduce the memory footprint by partitioning the data in all three dimensions. We see in Tab. 2 that our approach achieves similar reconstruction performance as the unrolled 3D network, while using significantly less memory during training. When using patch-training, we either use patches of size 128^2 for 2D networks or 8×128^2 for 3D networks. We provide more details on the influence of the patch size in Appendix C.

5.3. Ablation study

We conduct an ablation study (Tab. 3) to assess the individual contributions of our proposed domain partitioning strategy and normal operator approximation technique.

Walnut-CBCT The size of the CBCT problem makes it impossible to evaluate the normal operator $A^\top A$ directly, thus we report no ablation for this setting. As reported in Tab. 3, the domain partitioning strategy enables the training of unrolled networks and yields state-of-the-art performance. When combined with the normal operator approximation, we observe that both the performance and the training speed are further improved, with a near 30% reduction in training time.

Calgary-Campinas MC-MRI In Tab. 3, we see that the

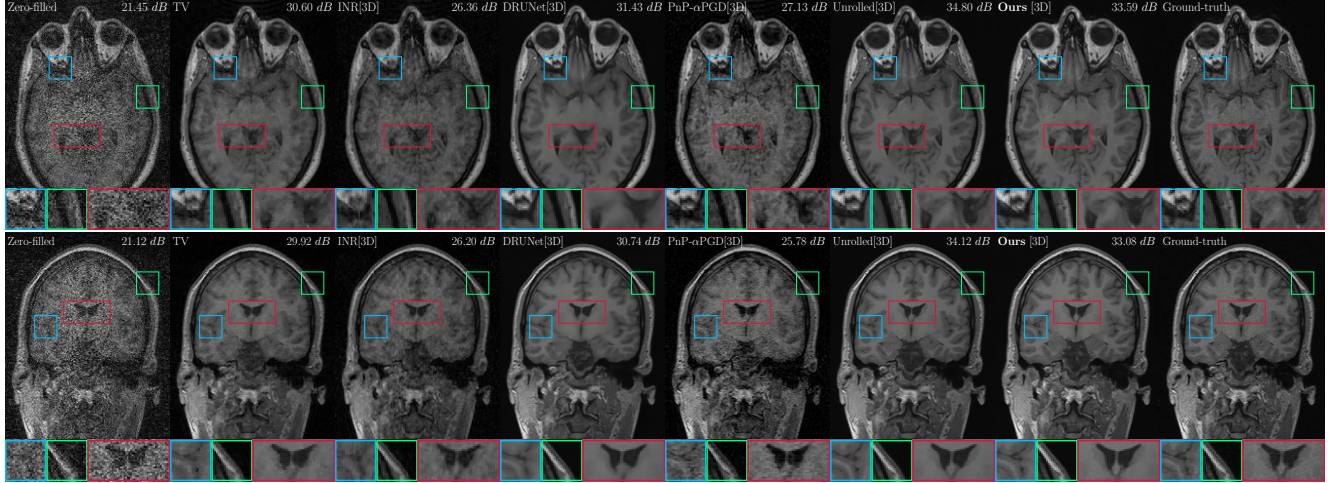


Figure 4. Illustrations of MC-MRI reconstructions with acceleration rate of 5 on the **Calgary-Campinas** dataset [52] for the methods compared in Tab. 2. *First row:* axial slice, *second row:* coronal slice from the same sample. PSNR is computed per slice.

domain partitioning strategy allows us to divide the memory footprint by a factor of 2 while maintaining similar reconstruction performance (-0.38 dB in PSNR). Naturally, it also reduces the training time per step, as smaller patches require fewer computations.

As opposed to CBCT, the normal operator in MC-MRI already relies on efficient FFT computations. Indeed, we observe that the original data-step in MC-MRI only accounts for 5% of the forward step, thus limiting the potential speed-up. As explained in Remark 4.3, we observe a drop in performance (Tab. 3) when using the normal operator approximation alone, although it still remains second best among compared methods. We expect the approximation to bring more significant benefits in Non-Cartesian MRI settings [45], where the normal operator is much more expensive to compute.

Table 3. Ablation study on the **Calgary-Campinas** dataset and the **Walnut-CBCT** dataset. For each line we report the PSNR averaged on the different subsampling configurations, as well as the peak video memory usage in GB and training speed. **Best** and **second-best** results highlighted.

Configuration	Calgary MC-MRI			Walnut-CBCT		
	PSNR ↑	VRAM ↓	s/step ↓	PSNR ↑	VRAM ↓	s/step ↓
Unrolled [3D]	36.23	75.93	2.16	✗	OOM	✗
→ w. $\mathbf{A}^\top \mathbf{A}$ approximation	35.12	74.48	2.15	✗	OOM	✗
→ w. partitioning	35.85	37.02	1.10	34.11	44.70	1.65 × 4
→ w. part. + $\mathbf{A}^\top \mathbf{A}$ approx.	35.09	37.04	1.09	34.15	44.70	1.21 × 4

6. Limitations

In this work, we focus on inverse problems with Gaussian noise models, where the data-consistency step involves evaluating the normal operator $\mathbf{A}^\top \mathbf{A}$ to minimize a least-squares

objective. While Poisson noise model is more appropriate for certain modalities such as low-dose CT, and does not rely on evaluating the normal operator, previous works have shown that unrolled networks designed for Gaussian noise models demonstrate state-of-the-art performance even under non-Gaussian noise conditions [2, 20, 60]. Therefore, our proposed techniques remain relevant for a wide range of inverse problems beyond those strictly adhering to Gaussian noise assumptions.

7. Conclusion

In this work, we address the challenge of scaling unrolled networks for large-scale inverse problems by introducing two key techniques: domain partitioning and normal operator approximation. The domain partitioning strategy decomposes large-scale inverse problems into smaller subproblems, yielding lower memory complexity at train-time. This approach extends patch-based training methods to unrolled architectures, ensuring scalability without compromising performance. Our proposed normal operator approximation completes our previous technique and replaces its evaluation with a product of diagonal and circulant matrices, enabling efficient data-consistency updates via the FFT. This reduces computational overhead, making it feasible to train and deploy unrolled networks for large-scale problems. We validate our approach through extensive experiments on 3D CBCT and 3D multi-coil accelerated MRI, demonstrating state-of-the-art performance while significantly reducing resource requirements. Notably, our method handles volumes as large as 501^3 on a single GPU, highlighting its potential for practical deployment in resource-constrained environments.

Acknowledgements

R. Vo and J. Tachella acknowledge support by the French National Research Agency (Agence Nationale de la Recherche) grant UNLIP (ANR-23-CE23-0013). This project was provided with computing HPC and storage resources by GENCI at IDRIS thanks to the grant 2025-AD011014958R1 on the supercomputer Jean Zay's V100 and H100 partitions.

References

[1] Jonas Adler and Ozan Öktem. Solving ill-posed inverse problems using iterative deep neural networks. *Inverse Problems*, 2017. 1, 2, 3

[2] Jonas Adler and Ozan Öktem. Learned primal-dual reconstruction. *IEEE Transactions on Medical Imaging*, 2018. 1, 6, 8

[3] Hemant Kumar Aggarwal, Merry P. Mani, and Mathews Jacob. MoDL: Model Based Deep Learning Architecture for Inverse Problems. *IEEE Transactions on Medical Imaging*, 2019. 2, 6

[4] Shaojie Bai, J. Zico Kolter, and Vladlen Koltun. Deep Equilibrium Models. In *Advances in Neural Information Processing Systems*, 2019. 1

[5] Amir Beck and Marc Teboulle. A Fast Iterative Shrinkage-Thresholding Algorithm for Linear Inverse Problems. *SIAM Journal on Imaging Sciences*, 2009. 1, 2

[6] Jérôme Bolte, Shoham Sabach, and Marc Teboulle. Proximal alternating linearized minimization for nonconvex and nonsmooth problems. *Mathematical Programming*, 2014. 3

[7] Hyungjin Chung, Dohoon Ryu, Michael T. McCann, Marc L. Klasky, and Jong Chul Ye. Solving 3D Inverse Problems Using Pre-Trained 2D Diffusion Models. In *IEEE Conf. Comput. Vis. Pattern Recog.*, 2023. 2

[8] Regev Cohen, Michael Elad, and Peyman Milanfar. Regularization by Denoising via Fixed-Point Projection (RED-PRO). *SIAM Journal on Imaging Sciences*, 2021. 2

[9] Patrick L. Combettes and Jean-Christophe Pesquet. *Proximal Splitting Methods in Signal Processing*, pages 185–212. Springer New York, 2011. 3

[10] Henri Der Sarkissian, Felix Lucka, Maureen van Eijnatten, Giulia Colacicco, Sophia Bethany Coban, and Kees Joost Batenburg. A cone-beam X-ray computed tomography data collection designed for machine learning. *Scientific Data*, 2019. 7, 1

[11] Qiaqiao Ding, Gaoyu Chen, Xiaoqun Zhang, Qiu Huang, and Hui Jiand Hao Gao. Low-Dose CT with Deep Learning Regularization via Proximal Forward Backward Splitting. *Physics in Medicine & Biology*, 2020. 3, 6

[12] Alexey Dosovitskiy, Lucas Beyer, Alexander Kolesnikov, Dirk Weissenborn, Xiaohua Zhai, Thomas Unterthiner, Mostafa Dehghani, Matthias Minderer, Georg Heigold, Sylvain Gelly, Jakob Uszkoreit, and Neil Houlsby. An image is worth 16x16 words: Transformers for image recognition at scale. In *International Conference on Learning Representations*, 2021. 2

[13] Emilien Dupont, Hyunjik Kim, S. M. Ali Eslami, Danilo Jimenez Rezende, and Dan Rosenbaum. From data to functa: Your data point is a function and you can treat it like one. In *Int. Conf. Mach. Learn.*, 2023. 3

[14] Michael Elad. *Sparse and Redundant Representations: From Theory to Applications in Signal and Image Processing*. Springer New York, 2010. 3

[15] L. A. Feldkamp, L. C. Davis, and J. W. Kress. Practical cone-beam algorithm. *Journal of the Optical Society of America*, 1984. 6

[16] Jeffrey A. Fessler. *Analytical Tomographic Image Reconstruction Methods*. 2021. 5

[17] Samy Wu Fung, Howard Heaton, Qiuwei Li, Daniel McKenzie, Stanley Osher, and Wotao Yin. JFB: Jacobian-Free Back-propagation for Implicit Networks. In *AAAI Conference on Artificial Intelligence*, 2022. 1

[18] Pascal Getreuer. Rudin-Osher-Fatemi Total Variation Denoising using Split Bregman. *Image Processing On Line*, 2012. 3, 6

[19] Davis Gilton, Gregory Ongie, and Rebecca Willett. Deep Equilibrium Architectures for Inverse Problems in Imaging. *IEEE Transactions on Computational Imaging*, 2021. 1

[20] Abhiram Gnanasambandam, Yash Sanghvi, and Stanley H. Chan. The secrets of non-blind poisson deconvolution. *IEEE Transactions on Computational Imaging*, 2024. 8

[21] Yo Seob Han, Jaejun Yoo, and Jong Chul Ye. Deep Residual Learning for Compressed Sensing CT Reconstruction via Persistent Homology Analysis. 2016. 2, 6

[22] Andreas Hauptmann, Felix Lucka, Marta Betcke, Nam Huynh, Jonas Adler, Ben Cox, Paul Beard, Sébastien Ourselin, and Simon Arridge. Model-based learning for accelerated, limited-view 3-d photoacoustic tomography. *IEEE Transactions on Medical Imaging*, 2018. 2

[23] Andreas Hauptmann, Subhadip Mukherjee, Carola-Bibiane Schönlieb, and Ferdia Sherry. Convergent Regularization in Inverse Problems and Linear Plug-and-Play Denoisers. *Foundations of Computational Mathematics*, 2024. 1

[24] Jonathan Ho, Ajay Jain, and Pieter Abbeel. Denoising Diffusion Probabilistic Models. In *Advances in Neural Information Processing Systems*, 2020. 2

[25] Samuel Hurault, Antonin Chambolle, Arthur Leclaire, and Nicolas Papadakis. A relaxed proximal gradient descent algorithm for convergent plug-and-play with proximal denoiser. In *International Conference on Scale Space and Variational Methods in Computer Vision*, 2023. 6

[26] Michael Kellman, Kevin Zhang, Eric Markley, Jon Tamir, Emrah Bostan, Michael Lustig, and Laura Waller. Memory-Efficient Learning for Large-Scale Computational Imaging. *IEEE Transactions on Computational Imaging*, 2020. 2

[27] Diederik P. Kingma and Jimmy Ba. Adam: A Method for Stochastic Optimization. 2014. 1

[28] Maximilian B. Kiss, Ander Biguri, Zakhar Shumaylov, Ferdia Sherry, K. Joost Batenburg, Carola-Bibiane Schönlieb, and Felix Lucka. Benchmarking learned algorithms for computed tomography image reconstruction tasks. *Applied Mathematics for Modern Challenges*, 2025. 3

[29] Quoc-Tung Le, Elisa Riccietti, and Remi Gribonval. Spurious Valleys, NP-Hardness, and Tractability of Sparse Matrix Factorization with Fixed Support. *SIAM Journal on Matrix Analysis and Applications*, 2023. 3

[30] Dongwook Lee, Jaejun Yoo, Sungho Tak, and Jong Chul Ye. Deep Residual Learning for Accelerated MRI Using Magnitude and Phase Networks. *IEEE Transactions on Biomedical Engineering*, 65, 2018. 2, 6

[31] Johannes Leuschner, Maximilian Schmidt, Daniel Otero Baquer, and Peter Maaß. The LoDoPaB-CT Dataset: A Benchmark Dataset for Low-Dose CT Reconstruction Methods. *Scientific Data*, 2021. 1, 2

[32] Johannes Leuschner, Maximilian Schmidt, Poulami Somanya Ganguly, Vladyslav Andriashen, Sophia Bethany Coban, Alexander Denker, Dominik Bauer, Amir Hadjifaradji, Kees Joost Batenburg, Peter Maass, and Maureen van Eijndten. Quantitative Comparison of Deep Learning-Based Image Reconstruction Methods for Low-Dose and Sparse-Angle CT Applications. *Journal of Imaging*, 2021. 2

[33] Rui long Li, Matthew Tancik, and Angjoo Kanazawa. NerfAcc: A General NeRF Acceleration Toolbox. 2022. 1

[34] Jiaming Liu, Xiaojian Xu, Weijie Gan, Shirin Shoushtari, and Ulugbek Kamilov. Online Deep Equilibrium Learning for Regularization by Denoising. In *Advances in Neural Information Processing Systems*, 2022. 1

[35] Sebastian Lunz, Ozan Öktem, and Carola-Bibiane Schönlieb. Adversarial Regularizers in Inverse Problems. In *Advances in Neural Information Processing Systems*, 2018. 2

[36] Stephane Mallat. A wavelet tour of signal processing. 3

[37] Ben Mildenhall, Pratul P. Srinivasan, Matthew Tancik, Jonathan T. Barron, Ravi Ramamoorthi, and Ren Ng. NeRF: Representing Scenes as Neural Radiance Fields for View Synthesis. In *European Conference on Computer Vision*, 2020. 2

[38] Subhadip Mukherjee, Andreas Hauptmann, Ozan Öktem, Marcelo Pereyra, and Carola-Bibiane Schönlieb. Learned Reconstruction Methods With Convergence Guarantees: A survey of concepts and applications. *IEEE Signal Processing Magazine*, 2023. 1, 2

[39] Thomas Müller. tiny-cuda-nn, 2021. 1, 2

[40] Thomas Müller, Alex Evans, Christoph Schied, and Alexander Keller. Instant neural graphics primitives with a multiresolution hash encoding. *ACM Transactions on Graphics*, 2022. 2, 6, 1

[41] Minh Hai Nguyen and Pierre Weiss. Comparing Plug-and-Play and Unrolled networks. 2024. 1

[42] Adam Paszke, Sam Gross, Francisco Massa, Adam Lerer, James Bradbury, Gregory Chanan, Trevor Killeen, Zeming Lin, Natalia Gimelshein, Luca Antiga, Alban Desmaison, Andreas Kopf, Edward Yang, Zachary DeVito, Martin Raison, Alykhan Tejani, Sasank Chilamkurthy, Benoit Steiner, Lu Fang, Junjie Bai, and Soumith Chintala. Pytorch: An imperative style, high-performance deep learning library. In *Adv. Neural Inform. Process. Syst.*, 2019. 6

[43] Jean-Christophe Pesquet, Audrey Repetti, Matthieu Terris, and Yves Wiaux. Learning Maximally Monotone Operators for Image Recovery. *SIAM Journal on Imaging Science*, 2021. 2

[44] Nicola Pezzotti, Sahar Yousefi, Mohamed S. Elmahdy, Jeroen Hendrikus Fransiscus Van Gemert, Christophe Schuelke, Mariya Doneva, Tim Nielsen, Sergey Kastrulyin, Boudewijn P. F. Lelieveldt, Matthias J. P. Van Osch, Elwin De Weerd, and Marius Staring. An adaptive intelligence algorithm for undersampled knee mri reconstruction. *IEEE Access*, 2020. 1, 2

[45] Zaccharie Ramzi, Chaithya G R, Jean-Luc Starck, and Philippe Ciuci. Nc-pdnet: A density-compensated unrolled network for 2d and 3d non-cartesian mri reconstruction. *IEEE Transactions on Medical Imaging*, 2022. 8

[46] Olaf Ronneberger, Philipp Fischer, and Thomas Brox. U-Net: Convolutional Networks for Biomedical Image Segmentation. In *Medical Image Computing and Computer-Assisted Intervention*, 2015. 2

[47] Jevgenija Rudzusika, Buda Bajic, Ozan Öktem, Carola-Bibiane Schönlieb, and Christian Etman. Invertible learned primal-dual. In *NeurIPS 2021 Workshop on Deep Learning and Inverse Problems*, 2021. 2

[48] Michael E. Sander, Pierre Ablin, Mathieu Blondel, and Gabriel Peyré. Momentum Residual Neural Networks. In *International Conference on Machine Learning*, 2021. 2

[49] Michael Schmid, Rainer Steinwandt, Jörn Müller-Quade, Martin Rötteler, and Thomas Beth. Decomposing a matrix into circulant and diagonal factors. *Linear Algebra and its Applications*, 2000. 2, 3, 5

[50] Liyue Shen, John Pauly, and Lei Xing. NeRP: Implicit Neural Representation Learning With Prior Embedding for Sparsely Sampled Image Reconstruction. *IEEE Transactions on Neural Networks and Learning Systems*, 2022. 2

[51] Yang Song, Liyue Shen, Lei Xing, and Stefano Ermon. Solving inverse problems in medical imaging with score-based generative models. In *International Conference on Learning Representations*, 2022. 2

[52] Roberto Souza, Oeslle Lucena, Julia Garrafa, David Gobbi, Marina Saluzzi, Simone Appenzeller, Letícia Rittner, Richard Frayne, and Roberto Lotufo. An open, multi-vendor, multi-field-strength brain MR dataset and analysis of publicly available skull stripping methods agreement. *NeuroImage*, 2018. 7, 8, 1

[53] Anuroop Sriram, Jure Zbontar, Tullie Murrell, Aaron Defazio, C. Lawrence Zitnick, Nafissa Yakubova, Florian Knoll, and Patricia Johnson. End-to-end variational networks for accelerated mri reconstruction. In *Medical Image Computing and Computer Assisted Intervention*, 2020. 1, 3, 6

[54] Yu Sun, Jiaming Liu, and Ulugbek Kamilov. Block Coordinate Regularization by Denoising. In *Advances in Neural Information Processing Systems*, 2019. 4

[55] Yu Sun, Brendt Wohlberg, and Ulugbek S. Kamilov. An Online Plug-and-Play Algorithm for Regularized Image Reconstruction. *IEEE Transactions on Computational Imaging*, 2019. 2

[56] Yu Sun, Jiaming Liu, Mingyang Xie, Brendt Wohlberg, and Ulugbek S. Kamilov. CoIL: Coordinate-Based Internal Learning for Tomographic Imaging. *IEEE Transactions on Computational Imaging*, 2021. 2

[57] Julián Tachella, Matthieu Terris, Samuel Hurault, Andrew Wang, Dongdong Chen, Minh-Hai Nguyen, Maxime Song, Thomas Davies, Leo Davy, Jonathan Dong, Paul Escande, Johannes Hertwich, Zhiyuan Hu, Tobías I. Liaudat, Nils Laurent,

Brett Levac, Mathurin Massias, Thomas Moreau, Thibaut Modrzyk, Brayan Monroy, Sebastian Neumayer, Jérémie Scanvic, Florian Sarron, Victor Sechaud, Georg Schramm, Romain Vo, and Pierre Weiss. DeepInverse: A Python package for solving imaging inverse problems with deep learning. 2025. [6](#), [1](#)

[58] Matthew Tancik, Pratul Srinivasan, Ben Mildenhall, Sara Fridovich-Keil, Nithin Raghavan, Utkarsh Singhal, Ravi Ramamoorthi, Jonathan Barron, and Ren Ng. Fourier Features Let Networks Learn High Frequency Functions in Low Dimensional Domains. In *Adv. Neural Inform. Process. Syst.*, 2020. [2](#)

[59] Junqi Tang, Subhadip Mukherjee, and Carola-Bibiane Schönlieb. Accelerating Deep Unrolling Networks via Dimensionality Reduction. 2022. [2](#)

[60] Matthieu Terris, Samuel Hurault, Maxime Song, and Julian Tachella. Reconstruct Anything Model: a lightweight foundation model for computational imaging. 2025. [2](#), [6](#), [8](#), [1](#)

[61] Wim Van Aarle, Willem Jan Palenstijn, Jan De Beenhouwer, Thomas Altantzis, Sara Bals, K. Joost Batenburg, and Jan Sijbers. The ASTRA Toolbox: A platform for advanced algorithm development in electron tomography. *Ultramicroscopy*, 2015. [6](#)

[62] Wim Van Aarle, Willem Jan Palenstijn, Jeroen Cant, Eline Janssens, Folkert Bleichrodt, Andrei Dabravolski, Jan De Beenhouwer, K. Joost Batenburg, and Jan Sijbers. Fast and flexible X-ray tomography using the ASTRA toolbox. *Optics Express*, 2016. [6](#)

[63] Singanallur V. Venkatakrishnan, Charles A. Bouman, and Brendt Wohlberg. Plug-and-Play priors for model based reconstruction. In *IEEE Global Conference on Signal and Information Processing*, 2013. [2](#), [6](#)

[64] Martin Vetterli, Jelena Kovačević, and Vivek K Goyal. *Foundations of Signal Processing*. Cambridge University Press, 2014. [2](#), [5](#)

[65] Romain Vo, Julie Escoda, Caroline Vienne, and Étienne De-cencière. Plug-and-Play Learned Proximal Trajectory for 3D Sparse-View X-Ray Computed Tomography. In *European Conference on Computer Vision*, 2024. [2](#), [6](#), [1](#)

[66] Shanshan Wang, Taohui Xiao, Qiegen Liu, and Hairong Zheng. Deep learning for fast mr imaging: A review for learning reconstruction from incomplete k-space data. *Biomedical Signal Processing and Control*, 2021. [2](#)

[67] Yiheng Xie, Towaki Takikawa, Shunsuke Saito, Or Litany, Shiqin Yan, Numair Khan, Federico Tombari, James Tompkin, Vincent Sitzmann, and Srinath Sridhar. Neural Fields in Visual Computing and Beyond. *Computer Graphics Forum*, 2022. [2](#)

[68] Syed Waqas Zamir, Aditya Arora, Salman Khan, Mu-nawar Hayat, Fahad Shahbaz Khan, and Ming-Hsuan Yang. Restormer: Efficient transformer for high-resolution image restoration. In *IEEE Conf. Comput. Vis. Pattern Recog.*, 2022. [2](#)

[69] Jure Zbontar, Florian Knoll, Anuroop Sriram, Tullie Murrell, Zhengnan Huang, Matthew J. Muckley, Aaron Defazio, Ruben Stern, Patricia Johnson, Mary Bruno, Marc Parente, Krzysztof J. Geras, Joe Katsnelson, Hersh Chandarana, Zizhao Zhang, Michal Drozdzał, Adriana Romero, Michael Rabbat, Pascal Vincent, Nafissa Yakubova, James Pinkerton, Duo Wang, Erich Owens, C. Lawrence Zitnick, Michael P. Recht, Daniel K. Sodickson, and Yvonne W. Lui. fastMRI: An Open Dataset and Benchmarks for Accelerated MRI, 2019. [1](#)

[70] Ruyi Zha, Yanhao Zhang, and Hongdong Li. NAF: Neural Attenuation Fields for Sparse-View CBCT Reconstruction. In *Medical Image Computing and Computer Assisted Intervention*, 2022. [2](#)

[71] Kai Zhang, Wangmeng Zuo, Shuhang Gu, and Lei Zhang. Learning deep cnn denoiser prior for image restoration. In *IEEE Conf. Comput. Vis. Pattern Recog.*, 2017. [2](#)

[72] Kai Zhang, Yawei Li, Wangmeng Zuo, Lei Zhang, Luc Van Gool, and Radu Timofte. Plug-and-play image restoration with deep denoiser prior. *IEEE Trans. Pattern Anal. Mach. Intell.*, 2022. [1](#), [2](#), [6](#)

[73] Léon Zheng, Elisa Riccietti, and Rémi Gribonval. Efficient Identification of Butterfly Sparse Matrix Factorizations. *SIAM Journal on Mathematics of Data Science*, 2023. [3](#)

[74] Yuanzhi Zhu, Kai Zhang, Jingyun Liang, Jiezhang Cao, Bihang Wen, Radu Timofte, and Luc Van Gool. Denoising Diffusion Models for Plug-and-Play Image Restoration. In *IEEE Conf. Comput. Vis. Pattern Recog.*, 2023. [2](#)

Efficient Unrolled Networks for Large-Scale 3D Inverse Problems

Supplementary Material

A. Details about training configurations

Every learned model in Tabs. 1 and 2 is trained following the same global configuration: we use Adam optimizer [27] with an initial learning rate of 10^{-4} . We train for 10^5 steps with a batch size of 4 (artificially increased via gradient accumulation if necessary). We use cosine annealing which decays the learning rate to 10^{-8} at the end of training.

Fitting the normal operator approximation. We fit the normal operator approximation $\mathbf{H}(\mathbf{m}, \lambda)$ on Gaussian random vectors. For each operator we train for 3000 steps with a batch size of 4 using Adam optimizer with a fixed learning rate of 2.10^{-2} for CBCT and 2.5×10^{-2} for MC-MRI.

A.1. Walnut-CBCT

The dataset [10] contains 42 CBCT volumes of different walnuts. Each acquisition contains 1200 radiographies of size 972×768 pixels, acquired over a full 360° circular trajectory. The reconstruction volumes have a size of 501^3 voxels. The ground-truth volumes are obtained by running an accelerated gradient descent scheme using the full-view data [10]. The train/val split contains 34 volumes, while the test split contains 8 volumes.

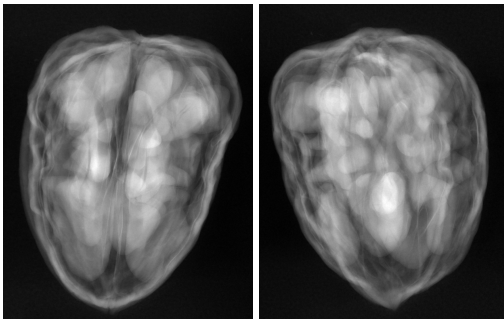


Figure 5. Illustrations of the **Walnut-CBCT** dataset. Examples of two radiographies.

DRUNet initialization. The 2D DRUNet [72] are initialized with the `deepinverse` weights [57]. During subsequent training, *i.e.* unrolling or post-processing, we fix the required noise value to $\sigma = 0.03$. The 3D DRUNet is initialized using the 2D DRUNet weights by inflating the 2D kernels to 3D. All kernels are of shape 3×3 , for an equivalent $3 \times 3 \times 3$ kernel, we copy the 2D weights to the central slice along the depth dimension and initialize the other slices with zeros. For upsampling and downsampling layers of shape 2×2 , we duplicate the 2D weights along the depth dimension to form $2 \times 2 \times 2$ kernels, and normalize them to preserve the

overall kernel norm.

Ours. Training **our** method, *i.e.* 3D DRUNet unrolled for $K = 3$ iterations with **domain partitioning** (cuboid patch size of 8×384^2) takes approximately 185 hours on a single NVIDIA H100 GPU with 80GB of video memory. Combining **domain partitioning** with **normal operator approximation** further reduces the training time to approximately 135 hours on the same hardware.

TV. We solve (2) with $g(x) = \|\nabla x\|_1$ using FISTA [5] for 1000 iterations with $\lambda = 0.2$, and step size $\eta = 1/L$, where L is the spectral norm of $\mathbf{A}^\top \mathbf{A}$ estimated via power iteration.

PnP- α PGD. For 2D and 3D, we respectively use the post-processing DRUNet trained on 2D slices and 3D patches as described above as the prior. More precisely, we run an accelerated PGD scheme [5] for $K = 40$ iterations with step size $\eta = 1.0/L$. For stability reasons, we relax the network evaluation with $\mathbf{D}_\alpha = (1 - \alpha)\mathbf{Id} + \alpha \mathbf{D}_\phi$, where \mathbf{D}_ϕ is the corresponding DRUNet. Similar to [65], we define $\alpha = \frac{\eta\lambda}{1+\eta\lambda}$, where λ is the weight of the implicit prior defined by the artifact removal network. We set $\lambda = 10$. for both 2D and 3D.

INR. Training an `instant-ngp` requires specific library dependencies. We use the specific CUDA implementation from `tiny-cuda-nn` [39] and the ray-casting code from `nerfacc` [33]. The INR uses a hash grid encoding [40] with 16 levels and a capacity of $T = 2^{21}$, a feature dimension of 2, a base resolution of 16, and a finest resolution of 256. The MLP has 2 hidden layers with 64 hidden units each. We train the INR by stochastic coordinate descent with Adam optimizer. The learning rate is initialized to 10^{-4} and decayed to 10^{-8} following a cosine scheduling for 25k steps. We cast 2048 rays per step, compute the associated data-fidelity for these rays and backpropagate the gradients to update the MLP and hash grid parameters.

DPIR[RAM]. We use the PnP Half-Quadratic Splitting (HQS) method from [72] with a Reconstruct Anything Model (RAM) prior [60]. We run it for $K = 20$ iterations, with $\lambda = 1/0.23$ and a decreasing noise schedule σ_k starting from $\sigma_1 = 49/255$. to $\sigma_K = 2.10^{-3}$.

A.2. Calgary-Campinas MC-MRI

The dataset [52] contains 59 fully-sampled Cartesian Multi-Coil MRI acquisitions of different brains. Each acquisition contains 12 coils with a k-space of size $256 \times 218 \times 170$. The k-space data is provided in a hybrid format, *i.e.* x-ky-kz, where a 1D FFT has already been applied along the

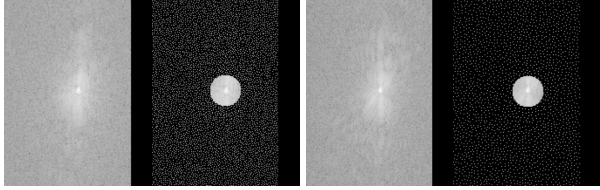


Figure 6. Illustrations of the **Calgary-Campinas** dataset. Examples of k-space measurements. (*left*) Slice of fully-sampled k-space (1st coil), and subsequently undersampled k-space with acceleration rate of 5. (*right*) Slice of fully-sampled k-space (1st coil) and, corresponding undersampled k-space with acceleration rate of 10.

frequency-encoded direction. The acceleration is performed along the phase encoding and slice encoding directions (k_y and k_z). This reduces the 3D problem to a set of independent 2D problems along the frequency-encoded direction (x), which allows us to train standard unrolled network without **domain partitioning**. We use a set of 48 samples for the train/val split and 21 samples for the test split. The ground-truth images are obtained by applying *root-sum-of-squares* (RSS) reconstruction on the fully-sampled k-space data. The sensitivity maps are estimated as in [44] by applying inverse FFT on the fully-sampled centered region of k-space data.

DRUNet initialization. The `deepinverse` library does not provide pretrained weights for complex data so both the 2D DRUNet and 3D DRUNet are trained from scratch.

Unrolled. As opposed to Walnut-CBCT, we can compare our method to a standard unrolled network without **domain partitioning** since the problem reduces to a set of independent 2D problems along the frequency-encoded direction (x). We use a sub-problem size of $8 \times 218 \times 170$ which maximizes VRAM usage during training. Training the 3D unrolled network for $K = 5$ iterations takes approximately 60 hours on a single NVIDIA H100 GPU with 80GB of video memory.

Ours. Training **our** method, *i.e.* 3D DRUNet unrolled for $K = 5$ iterations with **domain partitioning** (cuboid patch size of 8×128^2) takes approximately 17 hours and twice less memory than standard unrolling on a single NVIDIA H100 GPU with 80GB of video memory. Combining **domain partitioning** with **normal operator approximation** does not reduce training time as the original MC-MRI forward operator is already efficient to compute.

TV. We solve (2) with $g(x) = \|\nabla x\|_1$ using FISTA [5] for 1000 iterations with $\lambda = 7.4 \times 10^{-4}$, and step size $\eta = 1$, as the MC-MRI forward already has a spectral norm of 1.

PnP- α PGD. For 2D and 3D, we respectively use the post-processing DRUNet trained on 2D slices and 3D patches as described above as the prior. More precisely, we run an accelerated PGD scheme [5] for $K = 12$ iterations with step

size $\eta = 1.0$. For stability reasons, we relax the network evaluation with $D_\alpha = (1 - \alpha)\text{Id} + \alpha D_\phi$, where D_ϕ is the corresponding DRUNet. Similar to [65], we define $\alpha = \frac{\eta\lambda}{1 + \eta\lambda}$, where λ is the weight of the implicit prior defined by the artifact removal network. We set $\lambda = 2.10^{-6}$ for both 2D and 3D.

INR. As `tiny-cuda-nn` [39] does not natively support complex computation, required for FFT computations, we implement a similar grid-based INR architecture using PyTorch. The encoding is a latent grid of size 80^3 with 8 features on each vertex. The MLP has 2 hidden layers with 64 hidden units each. We train the INR by gradient descent with Adam optimizer for 1000 steps. The learning rate is fixed and set to $1e-2$. At each step we compute the data-fidelity on the full volume and backpropagate the gradients to update the MLP and grid parameters.

DPIR[RAM]. We use the PnP Half-Quadratic Splitting (HQS) method from [72] with a Reconstruct Anything Model (RAM) prior which natively provides the possibility to process complex data [60]. We run it for $K = 20$ iterations, with $\lambda = 1/0.23$ and a decreasing noise schedule σ_k starting from $\sigma_1 = 5.10^{-2}$ to $\sigma_K = 2.10^{-3}$.

B. Details about test-time configurations

In this section we detail the sub-procedure of Algorithm 1, *i.e.* the procedure to get \tilde{x} , namely we deploy a standard unrolling scheme by evaluating the prior on sequential patches.

We break each step (4) in $R_\phi(\mathbf{y}, \mathbf{A})$ as follows: **(i)** a first gradient descent step, computed on the full volume and full problem (1) $\mathbf{x}'_k = \mathbf{x}_k - \eta \nabla_{\mathbf{x}_k} d(\mathbf{A}\mathbf{x}_k, \mathbf{y})$, **(ii)** followed by a prior step on sequential patches, $\mathbf{x}_{k+1,p} = D_\phi(S_p \mathbf{x}'_k)$, where S_p extracts the p -th patch from the full volume. Finally, we aggregate the processed patches to form the full volume \mathbf{x}_{k+1} . We repeat this procedure for K iterations to get $\tilde{x} = \mathbf{x}_K$.

As opposed to training, this procedure is possible at test-time since we do not need to store activations for each processed patch, allowing us to process arbitrarily large volumes with limited memory.

Patch-based strategy. At test-time, we observe that the trained networks are robust to the choice of patch size. For **MC-MRI**, we only deploy a standard unrolling procedure and use patches of size $8 \times 218 \times 170$ with 3D methods and 218×170 with 2D methods, *i.e.* full spatial dimensions in $H \times W$. We either use a stride of size 4 along the depth dimension in 3D, or evaluate slice-by-slice in 2D. Then we aggregate to build a prediction of size $256 \times 218 \times 170$. For **CBCT**, we use two different strategies. When computing the estimation of the ground-truth \tilde{x} with the standard unrolling procedure, we use patches of size 8×501^2 with 3D methods and 501^2 with 2D methods. We either use a stride of size

4 along the depth dimension in 3D, or evaluate slice-by-slice in 2D. Then we aggregate to build a prediction of size 501^3 . In the second part, we deploy unrolling with domain partitioning and use patches of size 8×384^2 or 384^2 for 3D and 2D methods respectively.

Evaluation strategy. When evaluating the methods on the Walnut-CBCT dataset, we crop the ground-truth and predicted volumes to the central 300^3 voxels to avoid boundary artifacts and focus on part of the volumes that contains well-defined material.

C. Additional results

C.1. Influence of the patch size on the performances

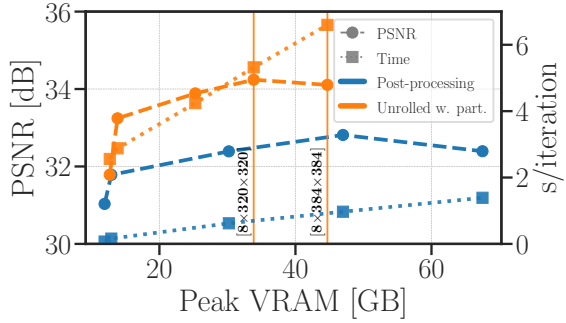


Figure 7. **Walnut-CBCT** - Average PSNR and time complexity against peak memory consumption during training. We vary the VRAM budget by changing the patch size used during domain partitioning. Larger patches lead to better performance at the cost of higher memory consumption. We do not show the complexity of standard unrolling (without partitioning) as a single H100 GPU is not sufficient for training it.

In Figs. 7 and 8 we provide the evolution of average PSNR and time complexity against peak memory consumption during training for different patch sizes on Walnut-CBCT and Calgary-Campinas MC-MRI datasets respectively.

We observe that larger patches lead to better performance at the cost of higher memory consumption. We note that on both dataset, for the same memory budget, our method with domain partitioning outperforms the standard post-processing. On Walnut-CBCT, we use patch sizes in $[(384 \times 384), (8 \times 128^2), (8 \times 256^2), (8 \times 320^2), (8 \times 384^2)]$, while on Calgary-Campinas MC-MRI, we use patch sizes in $[(218 \times 170), (8 \times 64^2), (8 \times 128^2), (8 \times 160^2), (8 \times 218 \times 170)]$.

Interestingly, we observe that on the MC-MRI experiment, performance starts to plateau for patch sizes larger than 8×128^2 , suggesting that the standard unrolling with no partitioning does not bring significant benefits compared to our method with domain partitioning for this specific problem and network complexity.

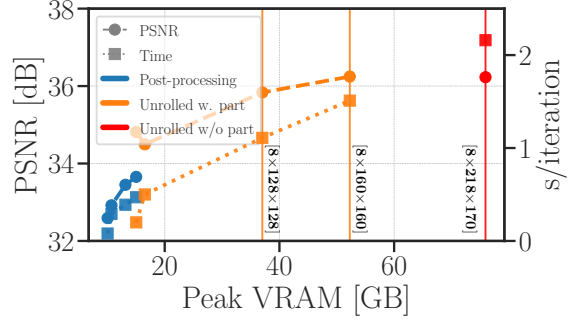


Figure 8. **Calgary-Campinas MC-MRI** - Average PSNR and time complexity against peak memory consumption during training. We vary the VRAM budget by changing the patch size used during domain partitioning. Larger patches lead to better performance at the cost of higher memory consumption.

C.2. Normal operator approximations

Walnut-CBCT. In Fig. 9, we provide additional illustrations of the normal operator approximation on Walnut-CBCT. We show a slice of the original volume \mathbf{x} , the exact normal operator evaluation $\mathbf{A}^\top \mathbf{A}\mathbf{x}$, and the approximated normal operator $\mathbf{H}(\mathbf{m}, \lambda)\mathbf{x}$. We see that λ , which corresponds to a filter in the Fourier domain, exhibits patterns predicted by the Fourier slice theorem, *i.e.* it performs sampling along radial directions.

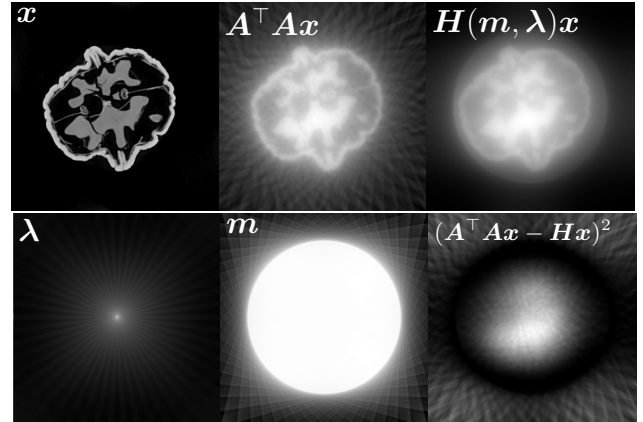


Figure 9. Illustrations of the normal operator approximation on **Walnut-CBCT**. (top row) Original volume slice \mathbf{x} , exact normal operator evaluation $\mathbf{A}^\top \mathbf{A}\mathbf{x}$, and approximated normal operator $\mathbf{H}(\mathbf{m}, \lambda)\mathbf{x}$. (bottom row) Learned filter λ , learned mask \mathbf{m} , and squared approximation error $(\mathbf{A}^\top \mathbf{A}\mathbf{x} - \mathbf{H}\mathbf{x})^2$.

Calgary-Campinas MC-MRI. In Fig. 10, we provide additional illustrations of the normal operator approximation on Calgary-Campinas MC-MRI. We show a slice of the original volume $|\mathbf{x}|$, the exact normal operator evaluation $|\mathbf{A}^\top \mathbf{A}\mathbf{x}|$, and the approximated normal operator $|\mathbf{H}(\mathbf{m}, \lambda)\mathbf{x}|$. We see

that λ , which corresponds to a filter in the Fourier domain, performs the same Fourier masking operation as the original acceleration pattern (Fig. 6). The spatial modulation m performs an operation similar to coil sensitivity maps.

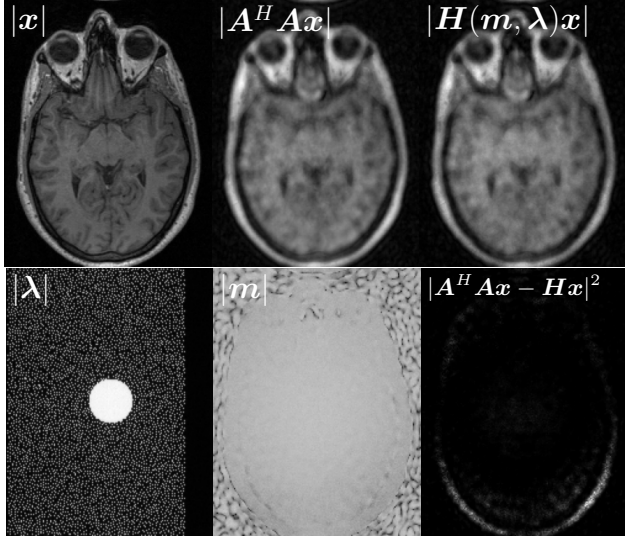


Figure 10. Illustrations of the normal operator approximation on **Calgary-Campinas**. (top row) Original volume slice $|x|$, exact normal operator evaluation $|A^H Ax|$, and approximated normal operator $|H(m, \lambda)x|$. (bottom row) Learned filter $|\lambda|$, learned mask $|m|$, and squared approximation error $|A^H Ax - Hx|^2$.